PHYSICAL REVIEW B **79**, 104102 (2009)

Indenter-angle-sensitive fracture modes and stress response at incipient plasticity

Zicheng Pan,[1] Hong Sun,[1,2,*] and Changfeng Chen[2,†]
[1]*Department of Physics, Shanghai Jiao Tong University, Shanghai 200240, China*
[2]*Department of Physics and High Pressure Science and Engineering Center, University of Nevada, Las Vegas, Nevada 89154, USA*

(Received 30 June 2008; revised manuscript received 3 October 2008; published 4 March 2009)

Determination of atomistic fracture modes under different loading conditions is essential to understanding nanomechanics. Here we report first-principles calculations that unveil intriguing indenter-angle-sensitive fracture modes and stress response at the incipient plasticity of strong covalent solids. We show that indenter-angle-dependent distributions of biaxial stresses beneath indenters can produce a variety of bond deformation and breaking patterns that are distinct, at different indenter angles, from each other and from those under a pure shear stress. These results provide key insights for understanding mechanisms of deformation and fracture modes probed by nanoindentation.

DOI: 10.1103/PhysRevB.79.104102 PACS number(s): 62.20.−x, 81.40.Jj

I. INTRODUCTION

Indentation measurement has been widely used as a standard test for material strength and hardness. Recent advances[1–7] in nanoscale control and imaging have made nanoindentation a versatile tool for material characterization beyond its original scope of hardness testing. Of particular interest is its ability to probe atomistic fracture modes responsible for incipient structural instability leading to the initial dislocation formation. Nanoindentation produces biaxial stress beneath the indenter with a shear stress and a normal compressive pressure component that can reach tens or even hundreds of gigapascals[2,8,9] ($1\ \mathrm{GPa}=10^9\ \mathrm{N/m^2}$). The limit of the structural stability of the specimen in nanoindentation is closely related to its maximum shear strength,[10] which precedes the initiation of cracks and dislocations that lead to plastic deformation.[11,12] Empirical engineering models employ scaling functions for stress-strain relations in structural mechanics and in the design of strong solids.[13] Recent advances[11,12,14–21] have made it possible to calculate directly the ideal shear strength, i.e., the shear stress at which a perfect crystal becomes mechanically unstable, which sets an upper bound for the material strength, using the density functional theory (DFT) based, highly accurate first-principles calculation methods. These calculations also provide atomistic deformation modes and accurate stress-strain relations which offer key insights into mechanisms responsible for fracture modes at incipient plasticity. However, in most of these previous ideal shear strength calculations,[11,12,14–21] compressive pressures under indenters normal to indentation crystal planes are neglected in the calculations, which gives rise to certain degrees of ambiguity when the calculated (pure) ideal shear strengths are compared to the hardness results obtained using different types of indenters under which different degrees of normal compressive pressures exist depending on the centerline-to-face angles of indenters.

In the present work, we address this fundamental issue in nanoscale structural mechanics as probed by nanoindentation, namely, the indenter angle dependence of atomistic fracture modes and stress response at incipient plasticity. It is known[22] that hardness by the conventional indentation method is not an accurately defined physical quantity, especially for brittle materials, since it depends on many nonuniform and uncontrolled factors such as indenter geometry, load, loading rate, and crack formation in indented material, among others. A more precise determination of intrinsic material strength can be achieved by measuring the ideal strength or yield strength that characterizes the initiation of plastic flow of the material. The latest experimental developments have demonstrated that ideal strength[23] and yield strength[24] can be directly measured through carefully designed procedures that avoid many of the pitfalls of conventional indentation methods.[23,24] However, indenter geometry, such as the indenter angle, remains a major factor that could influence inherent material response to applied loads and, therefore, requires a careful examination. In this work, we consider the effects of normal compressive pressures under indenters, which depend on the centerline-to-face angles of indenters and on the ideal shear stresses of strong covalent solids, cubic (*c*-) BN and $\mathrm{BC_2N}$. The results reveal a rich variety of bond deformation and breaking modes at different indenter angles, which shed light on atomistic mechanisms of fracture modes at incipient plasticity and provide insights for understanding material deformation behavior at nanoscale.

II. MODELING AND COMPUTATIONAL PROCEDURES

The total-energy calculations were carried out using the local-density approximation (LDA) pseudopotential scheme and a plane-wave basis set[25–27] with the PARATEC code.[28] The norm-conserving Troullier-Martins pseudopotentials[29] were used with cutoff radii of 1.3, 1.3, and 1.5 a.u. for N, C, and B, respectively. The exchange-correlation functional of Ceperley and Alder[26] as parametrized by Perdew and Zunger[30] was used. The total energy of the structures was minimized by relaxing the structural parameters using a quasi-Newton method.[31] The total-energy and stress calculations used an eight-atom zinc-blende-structured unit cell, an $8\times8\times8$ Monkhorst-Pack[32] *k*-point grid, and an 80 Ry energy cutoff. The resulted convergence in the calculated stresses was less than 0.1 GPa. The quasistatic ideal shear strength and relaxed loading path in easy slip (or cleavage) planes under

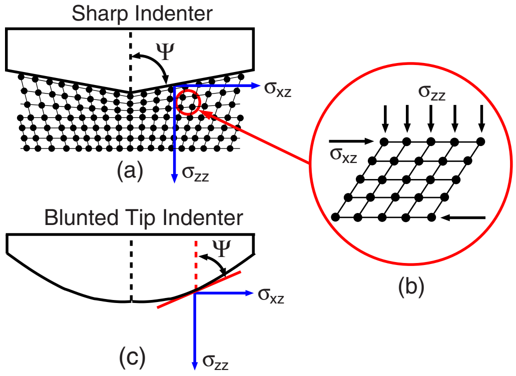

FIG. 1. (Color online) Illustration of the structural deformation under the stresses beneath the indenter. (a) A sharp indenter; (b) the microscopic (infinite and perfect) lattice of a macroscopically small volume beneath the indenter under uniform stress fields, σ_{xz} and σ_{zz}; and (c) an indenter with a blunted tip.

biaxial stress were determined using a method described previously[14,15] with additional constraints imposed by the indenter angle as discussed below.

Recent experiments revealed that results of nanoindentation depend sensitively on indenter geometry.[4,5] However, an understanding of the underlying mechanism is still lacking. Here we examine the atomistic response to nanoindentation by a sharp indenter with different centerline-to-face angle Ψ. We use sharp indenters in our calculations primarily because it is simple to explain how the normal compressive pressures under indenters are considered in our calculations. The results can be easily extended to indenters with blunted tips, which will be discussed at the end of the paper. We choose the Vickers and cube-corner indenter values of $\Psi=68°$ and 35.3° to represent large and small indenter angles, respectively. To describe the biaxial stress under the indenter, we decompose the contact force between the indenter face and the specimen into two components: F_x parallel to the specimen surface and F_z perpendicular to the surface. They project onto the same contact area and produce a pure shear stress component $\sigma_{xz}=F_x/A_z$ and a normal compressive pressure component $\sigma_{zz}=F_z/A_z$, where A_z is the projected area under the indenter. They are related by $\sigma_{zz}/\sigma_{xz}=\tan\Psi$, where Ψ is the centerline-to-face angle of the indenter, as shown in Fig. 1(a).

We also would like to address a general issue that concerns the differences in analyzing structural deformation from microscopic first-principles calculations and macroscopic theory in contact mechanics. In modeling the indenter process for first-principles calculations, we consider a small volume of the indented material as illustrated in Fig. 1(a). On a macroscopic scale, all the stresses (σ_{zz} and σ_{xz}, etc.) acting on this small volume can be regarded as uniform. Meanwhile, on a microscopic atomic scale this volume is large enough such that for the study of the bond breaking process one can formally regard it as an infinite and perfect lattice under a uniform stress field suitable for first-principles calculations [see Fig. 1(b)]. In our calculations, we study the lattice deformation of a chosen macroscopically small volume as the stress field (σ_{zz} and σ_{xz}, etc.) increases from zero to a value where atomic bond breaking (fracture) occurs. Contact mechanics solve the final equilibrium distribution of the stress field based on the continuum elastic stress field theory. A fracture or phase transformation would occur when the (final) stress obtained from the contact mechanics theory at a given point in the material beneath the indenter reaches or exceeds the atomic bond breaking stress obtained from the first-principles calculation. It would also indicate the breakdown of the elastic stress field theory used in the contact mechanics before the stresses become infinitely large.

Our first-principles calculation procedures are similar to those reported previously on the ideal shear strength calculations.[11,12,14–21] A chosen macroscopically small volume of the material beneath the indenter is approximated by a microscopically infinite and perfect lattice under a uniform stress field of shear stress σ_{xz} (as the x direction) and normal compressive pressure σ_{zz} (as the z direction), as indicated in Figs. 1(a) and 1(b). The quasistatic shear strength and relaxed loading path were determined by deforming the lattice vectors incrementally in the direction of the applied shear strain ϵ_{xz}. At each step, a small shear strain ($\Delta\epsilon_{xz}=0.005$) is applied in the chosen shear direction in the easy slip (or cleavage) plane and held fixed during the structural relaxation, which determines the calculated shear stress (σ_{xz}), while the other five independent components of the strain tensor and all the atoms inside the unit cell were simultaneously relaxed until (i) the compressive pressure normal to the easy slip plane reached a specified value [i.e., $\sigma_{zz}=\sigma_{xz}\tan\Psi$, where Ψ is the centerline-to-face angle of the indenter, see Fig. 1(a)], (ii) all the other four components (σ_{xx}, σ_{yy}, σ_{xy}, and σ_{yz}) of the Hellmann-Feynman stress tensor are negligible (less than 0.1 GPa), and (iii) the force on each atom becomes zero. The shape of the (deformed) unit cell and the relation between the shear stress σ_{xz} and shear strain ϵ_{xz} are determined completely at each step by this constrained atomic relaxation including the effect of σ_{zz}. If we set $\Psi=0$ (so $\sigma_{zz}=0$) in the calculation, it is equivalent to require all the five stress components (except σ_{xz}) become zero during the structural relaxation, which is the relaxation procedure used in previous calculations of pure ideal shear stresses[11,12,14–21] that neglect the effects of normal compressive pressures and geometry (indenter's angles) of indenters. We performed calculations on diamond, c-BN, and c-BC$_2$N that contain a variety of strong covalent bonds and provide an ideal testing ground for benchmark results. The calculated peak stress and strain and the bond breaking strain are listed in Table I. Considering diamond is usually the indenter instead of indented material, we focus below on the results of c-BN and two c-BC$_2$N phases.

III. RESULTS AND DISCUSSION

Figure 2 shows calculated stress-strain relations of c-BN under the biaxial stresses ($\Psi=35.3°$ and 68°) in comparison with that under pure shear stress ($\Psi=0°$). The indentation is applied to its easy cleavage (111) plane.[33] It is seen that the fracture modes at the incipient plasticity are highly sensitive to the indenter angle. At small Ψ (35.3°) the biaxial stress induces graphitization beyond the elastic limit with the graphitized BN layers aligned in the [111] direction perpen-

TABLE I. Calculated peak stress (σ_{max}), strain (ϵ_{max}), and bond breaking strain (ϵ_b) for diamond, *c*-BN, and HD-BC$_2$N and LD-BC$_2$N under pure shear stress, and biaxial stresses at indenter angles 35.3° and 68°, respectively, in the weakest shear directions.

	Diamond	*c*-BN	HD-BC$_2$N	LD-BC$_2$N
Pure shear	(111)[11$\bar{2}$]	(111)[11$\bar{2}$]	(111)[1$\bar{2}$1]	(111)[11$\bar{2}$]
σ_{max}	96.3	70.4	68.8	11.7
ϵ_{max}	0.345	0.370	0.265	0.085
ϵ_b	0.350	0.375	0.275	0.090
Biaxial (35.3°)	(111)[11$\bar{2}$]	(111)[11$\bar{2}$]	(111)[1$\bar{2}$1]	(111)[11$\bar{2}$]
σ_{max}	103	72.1	72.3	25.3
ϵ_{max}	0.360	0.385	0.285	0.185
ϵ_b	0.390	0.410	0.305	0.190
Biaxial (68°)	(111)[11$\bar{2}$]	(111)[11$\bar{2}$]	(111)[1$\bar{2}$1]	(111)[11$\bar{2}$]
σ_{max}	97.6	64.3	70.0	66.8
ϵ_{max}	0.300	0.385	0.275	0.220
ϵ_b	0.345	0.395	0.290	0.240

dicular to the specimen surface, which is in contrast to the situation under pure shear stress where the graphitized BN layers are aligned in the [11$\bar{2}$] direction parallel to the specimen surface. This difference is caused by the normal compressive pressure component that prevents the bond breaking and volume expansion in the [111] direction. Moreover, the shear component of the biaxial stress produces bond breaking along the [11$\bar{2}$] direction which occurs at a larger strain of 41% (see Table I) compared to 37.5% under pure shear stress, accompanied by a small increase in the peak stress. In stark contrast, at larger Ψ (68°), the fracture modes at the incipient plasticity are qualitatively different. Here the much larger normal compressive pressure component causes the collapse of the bonds aligned perpendicular to the specimen surface as indicated by the sharp decrease in the normal stress shown in the inset of the bottom panel of Fig. 1. This occurs when the [111] tensile contraction replaces the (111)[11$\bar{2}$] shear sliding as the preferred deformation mode since it has become the lowest-resistance path under the applied biaxial loading at large strains. Moreover, this drastically different fracture mode is accompanied by a significant reduction in peak stress from 72.1 GPa at Ψ=35.3° to 64.3 GPa at Ψ=68°.

We next examine the recently synthesized[34–36] high-density (HD) and low-density (LD) *c*-BC$_2$N that rival *c*-BN in measured hardness. Previous calculations[37,38] have identified the atomic structures of these two polymorphs which differ in their atomic arrangements in the unit cell; both have the (111) easy cleavage plane[20] as in the case of *c*-BN.[33] Figure 3 shows the calculated stress-strain relations for HD-BC$_2$N which contains the stronger C-C, B-N, B-C, and N-C bonds without any weaker B-B or N-N bonds.[37,38] There are notable differences in the fracture modes of HD-BC$_2$N compared to those for *c*-BN despite similarities in the overall trend. First, at small Ψ (35.3°) the graphitized BC$_2$N layers

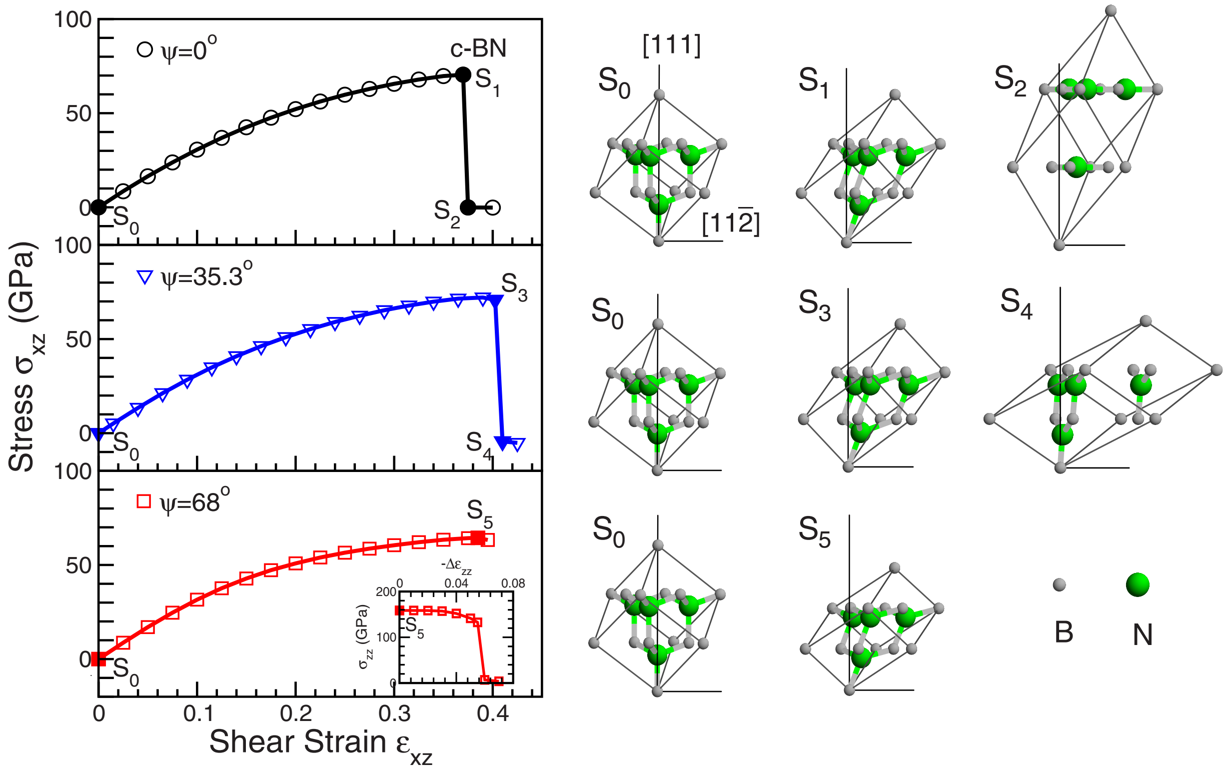

FIG. 2. (Color online) Calculated stress-strain relation and selected key bonding configurations for *c*-BN under pure shear stress (Ψ=0°), biaxial stress by cubic-corner indentation (Ψ=35.3°), and biaxial stress by Vickers indentation (Ψ=68°).

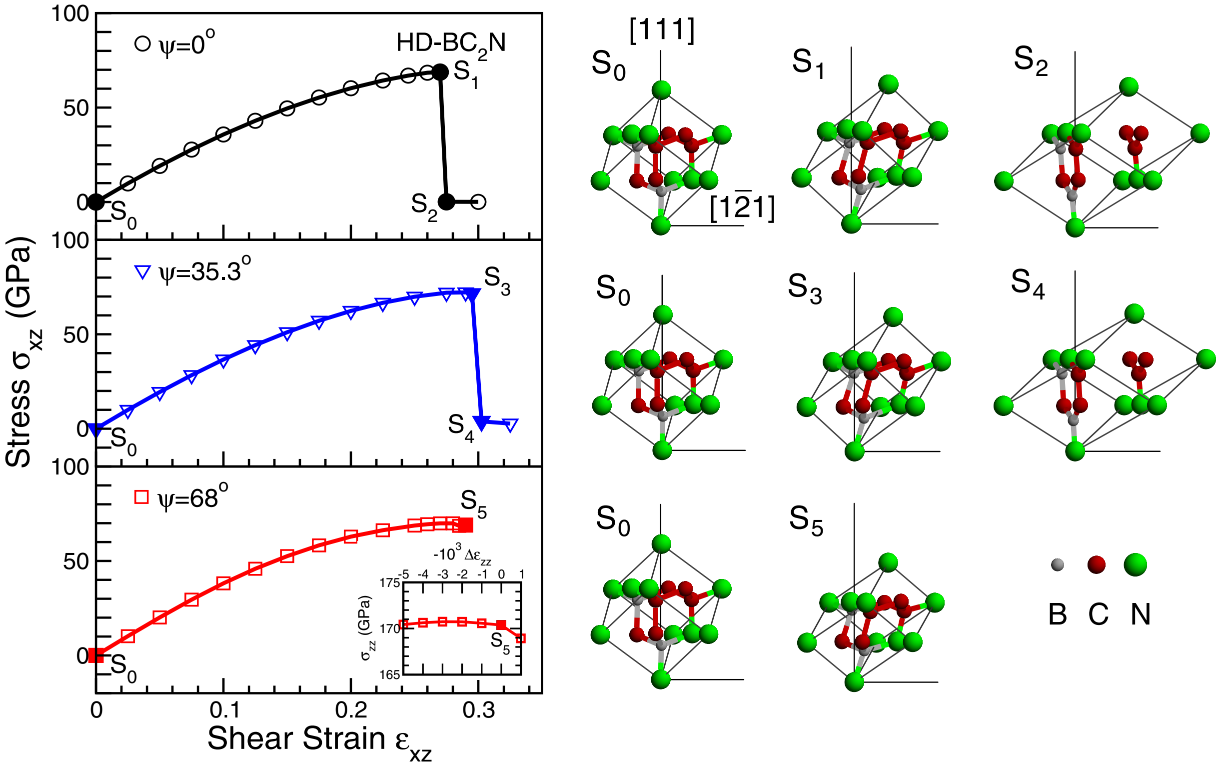

FIG. 3. (Color online) Calculated stress-strain relation and selected key bonding configurations for HD-BC$_2$N under the same deformation conditions as in Fig. 2.

are aligned in the same direction, perpendicular to the specimen surface, as under pure shear stress ($\Psi=0°$), and the increase in the peak shear stress is greater. Second, at larger Ψ (68°) the bond collapse under the normal stress component is not as precipitous, which is probably due to the presence of the less compressible B-C and C-N bonds along the [111] direction. Consequently, the peak stress remains at a high value of 70.0 GPa that is greater than that of *c*-BN under the same loading conditions. This is consistent with the Vickers indentation measurement[35] showing HD-BC$_2$N harder than *c*-BN.

More interestingly, LD-BC$_2$N presents an intriguing case of nanomechanical response that is highly sensitive to indenter angles. Compared to HD-BC$_2$N it has lower density, lower bulk modulus, and anomalous low sound velocities but high hardness.[36,39] A structure containing weak N-N bonds has been identified[37,38,40] to provide a consistent explanation for these properties. Here we explore the sensitivity of its fracture modes to indenter angle. Under pure shear stress ($\Psi=0°$), the B-C bonds that align parallel to the weak N-N bonds in the [111] direction break at a very low strain of 9% (see results in top panel of Fig. 4), resulting in a peak stress of only 11.7 GPa. At small Ψ (35.3°), the normal stress component prevents bond (and volume) expansion in the otherwise weakest [111] direction; the structure undergoes further shear deformation, leading to graphitization with the layered structures aligned basically in the indenter angle direction (see the structural snapshot in the middle panel of Fig. 4). This additional shear deformation yields a much higher peak stress of 25.3 GPa under $\Psi=35.3°$. In the two cases just examined, the weak N-N bonds play a dominant role in determining the overall fracture modes and in both cases the bond breaking occurs in the same direction as the original (pure shear) or tilted ($\Psi=35.3°$) N-N bonds. However, the situation changes significantly under the indentation with larger $\Psi=68°$. In this case, the much larger normal compressive pressure component causes the rebonding of the originally weak N-N bonds (see structural snapshots S_5 and S_6 in Fig. 4). It causes a drastic hardening of the structure which is able to sustain much larger shear deformation with a nearly sixfold enhancement in the peak stress (from 11.7 to 66.8 GPa). The bond breaking occurs in a direction almost perpendicular to the original weak N-N bonds. It demonstrates a case of extreme sensitivity of atomistic fracture modes and stress response at incipient plasticity.

Our results obtained with ideal sharp indenters can be easily extended to understand the real indentation processes where indenters generally have blunted tips. Figure 1(c) gives the sketch of a blunted tip indenter. One considers a small volume of the indented material beneath the indenter as illustrated in Fig. 1(a). The relation between the normal compressive pressure σ_{zz} and shear stress σ_{xz} beneath the indenter is $\sigma_{zz}=\sigma_{xz}\tan\Psi$, where Ψ now is the centerline-to-face-tangent-plane angle of the indenter [see Fig. 1(c)]. Materials at different locations beneath the indenter correspond to different angle Ψ. Obviously, for materials beneath the indenter near the centers of its faces, Ψ approaches that of an ideal sharp indenter, while for materials close to the tip, Ψ approaches 90°. In our calculations, we calculated ideal shear strengths with Ψ equal to those of two different sharp indenters (Vickers and cube-corner indenters), which are the smallest values of Ψ for indenters with blunted tips. The

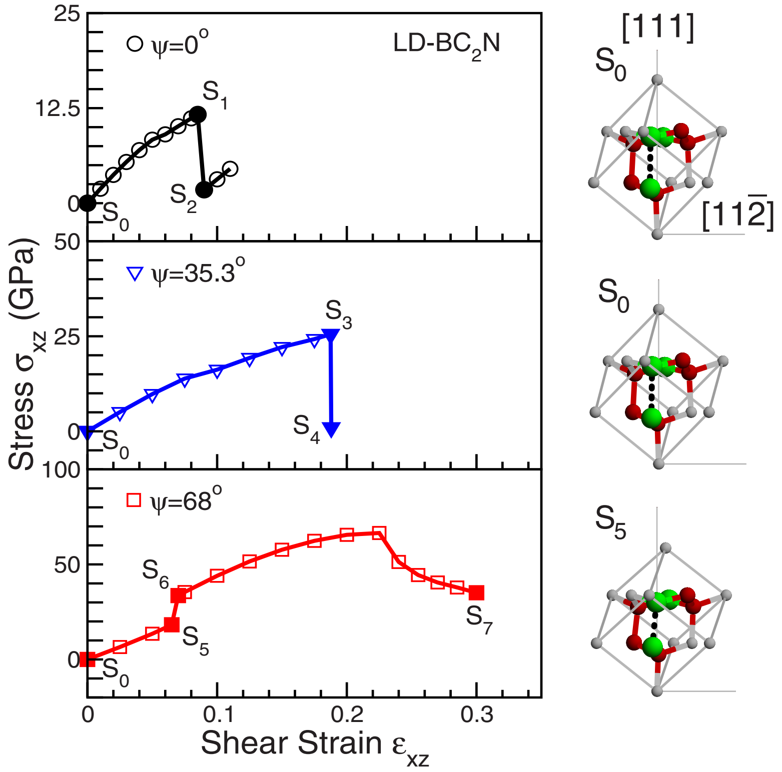

FIG. 4. (Color online) Calculated stress-strain relation and selected key bonding configurations for LD-BC$_2$N under the same deformation conditions as in Fig. 2. The black (thin) dashed lines connecting the atoms indicate pre-existing weak N-N bonds, while the red (thick) ones are the stress-induced broken bonds.

effects of normal compressive pressures under indenters on the indentation processes become increasingly important as Ψ increases since the ratio of $\sigma_{zz}=\sigma_{xz}\tan\Psi$ increases. If one knows the profile of an indenter, one can calculate Ψ at any point on the indenter's surface and uses the method described in our paper to determine ideal shear strengths of indented materials at different points beneath the indenter for different types of indenters. Even though the relations among different stresses in real situations under different indenters are much more complex, the simple relation between σ_{zz} and σ_{xz} we assumed allows us to capture the main physics, which shows the importance of the compressive pressures under indenters that will result in completely different structural deformation modes, new bond breaking patterns, and different (much higher) peak shear stresses compared to those obtained in the previous calculations[11,12,14–21] where σ_{zz} is neglected. In Figs. 2–4, we calculated ideal shear strengths with $\Psi=0°$, 35.3°, and 68°. The results can give a general trend on how the ideal shear strengths depend on the centerline-to-face-tangent-plane angle of indenters. Take a cubic-corner indenter with blunted tip as an example; near the centers of the indenter's faces the structural deformation modes, bond breaking patterns, and ideal shear stress of the indented material will behave like the results calculated with $\Psi=35.3°$; while close to the tips they will behave like those obtained with $\Psi=68°$ (or even larger Ψ).

Finally we highlight a significant impact on nanoindentation measurements by indenter-angle-sensitive fracture modes and stress response. Figure 5 shows calculated stress-strain relations for c-BN, HD-BC$_2$N, and LD-BC$_2$N. At $\Psi=35.3°$ the stress responses over the entire strain range up to incipient plasticity rank in descending order from HD-BC$_2$N to c-BN and then LD-BC$_2$N. This deviates from the ranking

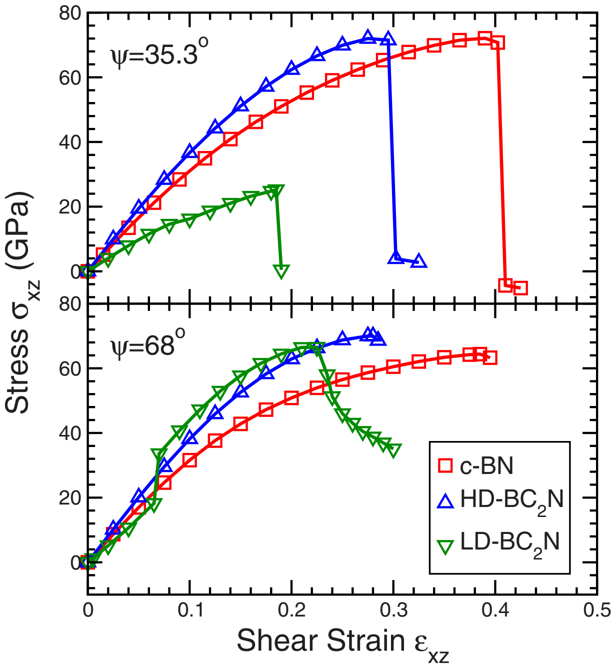

FIG. 5. (Color online) Comparison of the calculated stress-strain relations for c-BN, HD-BC$_2$N, and LD-BC$_2$N by nanoindentation with indenter angles of 35.3° and 68°, respectively.

order under pure shear stress (see Table I), namely, *c*-BN, HD-BC_2N, and LD-BC_2N although the quantitative differences are not large. However, at $\Psi=68°$, the order for stress responses becomes very sensitively dependent on strains: for strains below 7% it is (again in descending order) HD-BC_2N, *c*-BN, and LD-BC_2N, with their stresses close to each other; between strains of 7% and 22% it becomes LD-BC_2N, HD-BC_2N, and *c*-BN; and at strains above 22% it returns to the same order as at strains below 7% but with the stresses for the three materials well separated and the stress response of LD-BC_2N rapidly decreasing (although still more gradual compared to the nearly vertical drop under pure shear stress and at the small indenter angle). This complicated stress-strain behavior is driven by the indenter-angle-sensitive atomistic fracture modes that involve different bond breaking, graphitization, and constrained shear sliding patterns presented above. It demonstrates a high degree of intrinsic sensitivity of stress response in the indented material to indenter angle and applied strain. These results set key benchmarks for strong covalent solids and raise prospects of enabling analysis and understanding of delicate nanoscale fracture processes in a broad range of materials.

ACKNOWLEDGMENTS

This work was supported by the DOE Cooperative Agreement under Grant No. DE-FC52-06NA26274 at UNLV and National Natural Science Foundation of China under Grants No. 10874112 and No. 50532020.

---

*Corresponding author; hsun@sjtu.edu.cn

†Corresponding author; chen@physics.unlv.edu

[1] G. S. Smith, E. B. Tadmor, and E. Kaxiras, Phys. Rev. Lett. **84**, 1260 (2000).

[2] Y. G. Gogotsi, A. Kailer, and K. G. Nickel, Nature (London) **401**, 663 (1999).

[3] M. W. Barsoum, A. Murugaiah, S. R. Kalidindi, and T. Zhen, Phys. Rev. Lett. **92**, 255508 (2004).

[4] J. Jang, M. J. Lance, S. Wen, T. Y. Tsui, and G. M. Pharr, Acta Mater. **53**, 1759 (2005).

[5] H. Bei, E. P. George, J. L. Hay, and G. M. Pharr, Phys. Rev. Lett. **95**, 045501 (2005).

[6] Y. T. Cheng, W. Ni, and C. M. Cheng, Phys. Rev. Lett. **97**, 075506 (2006).

[7] C. Kearney, Z. Zhao, B. J. F. Bruet, R. Radovitzky, M. C. Boyce, and C. Ortiz, Phys. Rev. Lett. **96**, 255505 (2006).

[8] K. J. Van Vliet, J. Li, T. Zhu, S. Yip, and S. Suresh, Phys. Rev. B **67**, 104105 (2003).

[9] T. Zhu, J. Li, K. J. Van Vliet, S. Ogata, S. Yip, and S. Suresh, J. Mech. Phys. Solids **52**, 691 (2004).

[10] A. Gouldstone, H. J. Koh, K. Y. Zeng, A. E. Giannakopoulos, and S. Suresh, Acta Mater. **48**, 2277 (2000).

[11] S. Ogata, J. Li, and S. Yip, Science **298**, 807 (2002).

[12] S. Ogata, J. Li, N. Hirosaki, Y. Shibutani, and S. Yip, Phys. Rev. B **70**, 104104 (2004).

[13] V. V. Brazhkin, A. G. Lyapin, and R. J. Hemley, Philos. Mag. A **82**, 231 (2002).

[14] D. Roundy, C. R. Krenn, M. L. Cohen, and J. W. Morris, Jr., Philos. Mag. A **81**, 1725 (2001).

[15] D. Roundy, C. R. Krenn, M. L. Cohen, and J. W. Morris, Jr., Phys. Rev. Lett. **82**, 2713 (1999).

[16] H. Chacham and L. Kleinman, Phys. Rev. Lett. **85**, 4904 (2000).

[17] S. H. Jhi, S. G. Louie, M. L. Cohen, and J. W. Morris, Jr., Phys. Rev. Lett. **87**, 075503 (2001).

[18] D. M. Clatterbuck, C. R. Krenn, M. L. Cohen, and J. W. Morris, Jr., Phys. Rev. Lett. **91**, 135501 (2003).

[19] X. Blase, P. Gillet, A. San Miguel, and P. Mélinon, Phys. Rev. Lett. **92**, 215505 (2004).

[20] Y. Zhang, H. Sun, and C. F. Chen, Phys. Rev. Lett. **93**, 195504 (2004); **94**, 145505 (2005).

[21] M. G. Fyta, I. N. Remediakis, P. C. Kelires, and D. A. Papaconstantopoulos, Phys. Rev. Lett. **96**, 185503 (2006).

[22] V. Brazhkin, N. Dubrovinskaia, M. Nicol, N. Novikov, R. Riedel, V. Solozhenko, and Y. Zhao, Nature Mater. **3**, 576 (2004).

[23] T. Li, J. W. Morris, Jr., N. Nagasako, S. Kuramoto, and D. C. Chrzan, Phys. Rev. Lett. **98**, 105503 (2007).

[24] M. I. Eremets, I. A. Trojan, P. Gwaze, J. Huth, R. Boehler, and V. D. Blank, Appl. Phys. Lett. **87**, 141902 (2005).

[25] J. Ihm, A. Zunger, and M. L. Cohen, J. Phys. C **12**, 4409 (1979).

[26] D. M. Ceperley and B. J. Alder, Phys. Rev. Lett. **45**, 566 (1980).

[27] M. L. Cohen, Phys. Scr. **T1**, 5 (1982).

[28] See website (http://www.nersc.gov/projects/paratec/).

[29] N. Troullier and J. L. Martins, Phys. Rev. B **43**, 1993 (1991).

[30] J. P. Perdew and A. Zunger, Phys. Rev. B **23**, 5048 (1981).

[31] B. G. Pfrommer, M. Cote, S. G. Louie, and M. L. Cohen, J. Comput. Phys. **131**, 233 (1997).

[32] H. J. Monkhorst and J. D. Pack, Phys. Rev. B **13**, 5188 (1976).

[33] Y. Zhang, H. Sun, and C. F. Chen, Phys. Rev. B **73**, 144115 (2006).

[34] E. Knittle, R. B. Kaner, R. Jeanloz, and M. L. Cohen, Phys. Rev. B **51**, 12149 (1995).

[35] Y. S. Zhao, D. W. He, L. L. Daemen, T. D. Shen, R. B. Schwarz, Y. Zhu, D. L. Bish, J. Huang, J. Zhang, G. Shen, J. Qian, and T. W. Zerda, J. Mater. Res. **17**, 3139 (2002).

[36] V. L. Solozhenko, D. Andrault, G. Fiquet, M. Mezouar, and D. Rubie, Appl. Phys. Lett. **78**, 1385 (2001).

[37] H. Sun, S. H. Jhi, D. Roundy, M. L. Cohen, and S. G. Louie, Phys. Rev. B **64**, 094108 (2001).

[38] Z. C. Pan, H. Sun, and C. F. Chen, Phys. Rev. B **70**, 174115 (2004).

[39] S. N. Tkachev, V. L. Solozhenko, P. V. Zinin, M. H. Manghnani, and L. C. Ming, Phys. Rev. B **68**, 052104 (2003).

[40] Z. C. Pan, H. Sun, and C. F. Chen, Phys. Rev. Lett. **98**, 135505 (2007).